Influence of scintillation light confinement on depth-of-interaction measurement performance in a single-ended readout PET detector

Physics in Medicine & Biology

IPEM Institute of Physics and Engineering in Medicine

PAPER

Influence of scintillation light confinement on depth-of-interaction measurement performance in a single-ended readout PET detector

Hyeong Seok Shim[1,2,3], **Min Jeong Cho**[1,2,3], **Wen He**[4], **Min Sun Lee**[5], **Craig S Levin**[4,*] and **Jae Sung Lee**[1,2,3,*]

[1] Interdisciplinary Program in Bioengineering, College of Engineering, Seoul National University, Seoul, Republic of Korea
[2] Integrated Major in Innovative Medical Science, Seoul National University, Seoul, Republic of Korea
[3] Department of Nuclear Medicine, Seoul National University College of Medicine, Seoul, Republic of Korea
[4] Department of Radiology, Molecular Imaging Program, Stanford University, Stanford, California, United States of America
[5] Department of Electrica Engineering and Computer Science, Daegu Gyeongbuk Institute of Science and Technology, Daegu, Republic of Korea
* Authors to whom any correspondence should be addressed.

E-mail: cslevin@stanford.edu and jaes@snu.ac.kr

Keywords: positron emission tomography, depth-of-interaction, machine learning, maximum likelihood estimation

OPEN ACCESS

RECEIVED
18 January 2026

REVISED
17 April 2026

ACCEPTED FOR PUBLICATION
15 May 2026

PUBLISHED
1 June 2026

Abstract

Continuous depth-of-interaction (cDOI) detectors enable single-ended readout in positron emission tomography (PET) by encoding the interaction depth into the scintillation light distribution. This study presents a comprehensive performance optimization of a cDOI detector based on light distribution tailoring with crossed triangular-shaped reflectors by analyzing the effects of optical geometry based on various DOI decoding algorithms. Two parameters were systematically varied: the degree of light confinement through (1) optical segmentation and (2) crystal pitch adjustment. Five DOI decoding strategies—variance, max/sum ratio, Euclidean-distance classification, Gaussian and modified maximum-likelihood estimation, and artificial neural network (ANN) decoding—were adopted with 8 × 8 SiPM readout data. Results show that moderate segmentation (2 × 2 configuration) achieved the best DOI precision, yielding a 4.7 mm full width at half maximum (FWHM) and an ANN classification accuracy of 89 %. In the pitch study, 1.5 mm-pitch detector achieved better performance than 3.0 mm-pitch, indicating that increased optical interfaces allows more accurate encoding of the depth-dependent light distribution within the SiPM array. The ANN decoder consistently outperformed in DOI resolution compared to analytical and statistical methods by learning nonlinear spatial correlations among SiPM pixels. These findings highlight the coupled importance of optical geometry and data-driven decoding for achieving high DOI sensitivity in next-generation PET detector designs.

1. Introduction

In positron emission tomography (PET), the limited capability to measure the depth-of-interaction (DOI) within scintillation crystals often results in degraded spatial resolution, especially near the edges of the field of view (Ito *et al* 2011). When a 511 keV annihilation photon interacts with crystal at an unknown depth, the resulting parallax error causes the reconstructed line of response to deviate from its true position. Accurate DOI measurement can therefore improve spatial resolution uniformity by mitigating this geometric uncertainty. In addition, DOI information can help reduce the timing uncertainty of detected photons, which is becoming increasingly important in advanced time-of-flight PET systems (Seo *et al* 2023, Yi *et al* 2024).

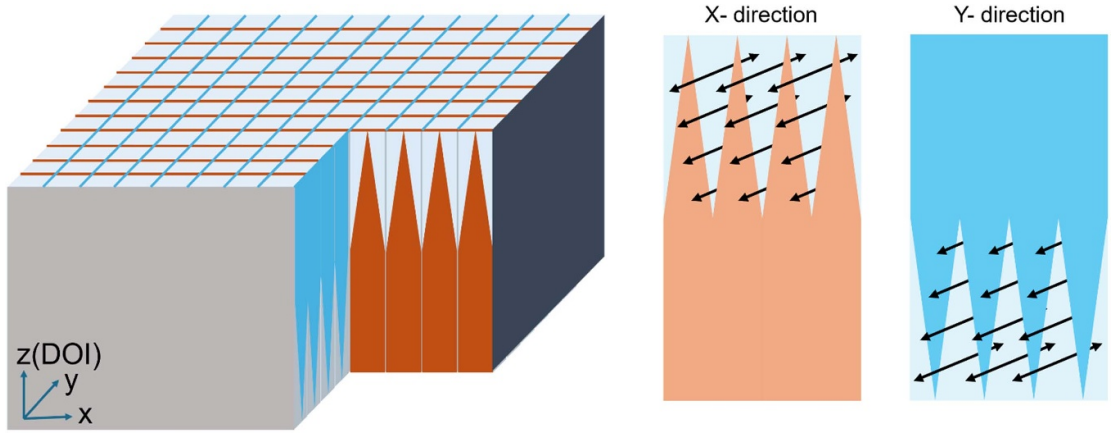

Figure 1. A continuous DOI (cDOI) PET detector using only a single-ended readout, in which DOI information is encoded in the light distribution measured by the photosensor array.

A variety of methods have been proposed to extract DOI information from PET detectors (Moses and Derenzo 1994, Lewellen *et al* 2004, Tsuda *et al* 2004, Hong *et al* 2008, Du *et al* 2009, Ito *et al* 2010a, Ito *et al* 2011, Son *et al* 2017, Du *et al* 2019, LaBella *et al* 2020a, 2020b, Yoshida *et al* 2021, Nadig *et al* 2023, Yu *et al* 2024). Among them, we previously proposed a method for measuring continuous DOI (cDOI) using only a single-ended readout, in which DOI information is encoded in the light distribution measured by the photosensor array (figure 1) (Ito *et al* 2010b, Ito *et al* 2013, Lee and Lee 2015, Lee *et al* 2017, Shim *et al* 2025). This approach tailors the internal light reflection pattern within a single-layer crystal array using crossed triangular-shaped reflectors. Depending on the depth of annihilation photon interaction within the crystal, scintillation light spreads preferentially along different axes with varying degrees of dispersion, enabling the DOI to be inferred from the measured light pattern.

This concept was initially demonstrated using a multi-anode photomultiplier tube and later refined using a digital silicon photomultiplier (dSiPM) (Ito *et al* 2013, Lee and Lee 2015). The dSiPM-based implementation achieved clear crystal identification and cDOI encoding, with an average DOI resolution of approximately 4 mm full-width at half-maximum (FWHM) (Lee and Lee 2015). A subsequent system-level prototype confirmed the applicability of this approach to an actual small-animal PET scanner, achieving sub-millimeter spatial resolution after DOI correction (Lee *et al* 2017).

Although these results demonstrated the feasibility of the method, further design optimization is required in several aspects, particularly regarding the extent of light spreading within the crystal array. While broader light sharing facilitates cDOI encoding, excessive spreading can obscure depth-dependent variations and degrade the signal-to-noise ratio, especially for edge crystals. It is therefore important to investigate whether confining scintillation light within a limited photosensor area can improve the DOI measurement performance.

In parallel, various decoding algorithms have been explored for our cDOI detectors. Conventional approaches, such as variance-based metrics or Gaussian maximum-likelihood estimation (MLE), rely on simplified statistical models of light transport (Ito *et al* 2010b, Ito *et al* 2013, Lee and Lee 2015). However, actual detector responses often deviate from these assumptions. More recently, data-driven techniques such as artificial neural networks (ANNs) have been introduced to model the nonlinear relationship between SiPM pixel intensities and interaction depth with greater flexibility, thereby improving DOI estimation performance (Shim *et al* 2025). A systemic comparison between these decoding algorithms is thus also necessary.

In this study, we present a comprehensive optimization of cDOI schemes by jointly examining the effects of detector's optical geometry and decoding algorithms. The main hypothesis tested here is that confining the lateral light spread enhances DOI precision. Such confinement can be achieved by either by segmenting crystal block with optical reflectors or by increasing the number of optical interfaces between scintillation crystals. To validate this hypothesis, multiple detector configurations were implemented and evaluated using five different decoding strategies—conventional analytical metrics, Euclidean-distance classification, Gaussian and modified MLE, and ANN-based decoding. By identifying the optimal combinations of optical geometry and DOI decoding method, this study establishes design principles that advance the performance of single-ended DOI detectors beyond previous cDOI implementations.

2. Materials and methods

As previously mentioned, our cDOI detection employs a single-ended readout scheme that estimates the annihilation photon interaction depth based on the spatial distribution of scintillation light within a continuous pixelated crystal (figure 1). Unlike discrete multi-layer DOI methods or dual-ended readout configurations, the cDOI approach does not rely on separated crystal layers or energy differences between two photosensors. Instead, it encodes depth information into the shape and width of the light-distribution pattern observed at the SiPM surface (Ito *et al* 2010a). As the interaction depth changes, the lateral spread of scintillation photons varies continuously, forming a depth-dependent light gradient that can be exploited for DOI estimation.

We investigated two different strategies to limit the light dispersion: (1) segmenting the array to directly confine light propagation, and (2) increasing optical interfaces by reducing the crystal pitch. To suppress other confounding effects, all detector configurations employed the same SiPM sensor, electronics, reflector, and optical coupling under an identical acquisition protocol. Two experimental scenarios were defined accordingly: scenario 1 varied the segmentation while fixing the crystal pitch at 2 mm to examine the effect of direct light confinement, whereas scenario 2 varied the crystal pitch under identical unsegmented conditions to investigate the effect of increased optical interfaces.

2.1. Detector configuration

In scenario 1, the influence of direct optical light confinement on DOI performance was investigated by introducing different levels of segmentation within a crystal array of fixed pitch. Three detector blocks were fabricated using 1200-grit-lapped LYSO crystals measuring 2 mm $\times$ 2 mm $\times$ 20 mm. Each block shared the same overall dimensions but differed in the degree of segmentation: (1) a single unsegmented 12 $\times$ 12 array, (2) a 2 $\times$ 2 segmented configuration composed of four 6 $\times$ 6 sub-arrays, and (3) a 4 $\times$ 4 segmented configuration composed of sixteen 3 $\times$ 3 sub-arrays (figure 2(a), table 1). Segmentation boundaries were formed using rectangular enhanced specular reflector (ESR, 3 M) films inserted between sub-arrays to restrict the lateral propagation of scintillation light. The segments were separated by an ESR reflector that fully covered the corresponding surfaces, thereby minimizing photon cross-talk between segments. Within each segment, the crystal pixels were partitioned by reflectors with triangular patterns along the X- and Y-directions, enabling controlled photon sharing with a depth-dependent magnitude. By confining photons to smaller optical regions while maintaining the same total detector area, these geometries allowed quantitative assessment of how directly limiting light spread influences DOI discriminability.

In scenario 2, the effect of increased optical interfaces was examined. Two crystal arrays were prepared with pitches of 1.5 mm and 3.0 mm, each consisting of 20 mm-long LYSO elements (figure 2(b)). An 8 $\times$ 8 SiPM array (S14160-3050HS-08, Hamamatsu Photonics, Japan) with a 3 mm pixel pitch served as the common photosensor. In all detectors, crystals were optically coupled to the SiPM using optical grease (BC-630, Saint-Gobain Crystals, France). All detector blocks were mounted on a custom mechanical holder to ensure consistent alignment between the crystal and SiPM arrays during optical coupling.

2.2. Experimental setup

All measurements were conducted under identical environmental and electronics conditions to ensure fair comparison among detector configurations. After coupling, each crystal array was enclosed within a light-tight mechanical housing to block external light. The operating temperature was maintained at 20 °C using an air cooling system to minimize SiPM gain variation during acquisition.

A ^{22}Na point source with an activity of approximately 17 μCi was used to generate 511 keV annihilation photons. A reference detector, composed of 1 mm-thick slab LYSO crystal, was placed opposite the tested detector to provide coincidence timing signals, ensuring that only true coincidence events were recorded (figure 3). The two detectors were aligned coaxially with their sensitive surfaces separated by approximately 30 cm.

Each detector block was mounted on a precision motorized translation stage that allowed controlled positioning along the beam axis. For scenario 1, measurements were performed at three representative depths—4, 10, and 16 mm from the SiPM surface—to capture variations in light distribution among the segmented geometries. For scenario 2, DOI-dependent responses were measured at five depths—2, 6, 10, 14, and 18 mm. The positioning accuracy of the translation stage was better than 0.1 mm, which is negligible compared with the expected DOI resolution. Although the number of irradiation points differed between the two scenarios, this difference does not affect the comparison because DOI performance metrics were compared only within each scenario, not between them.

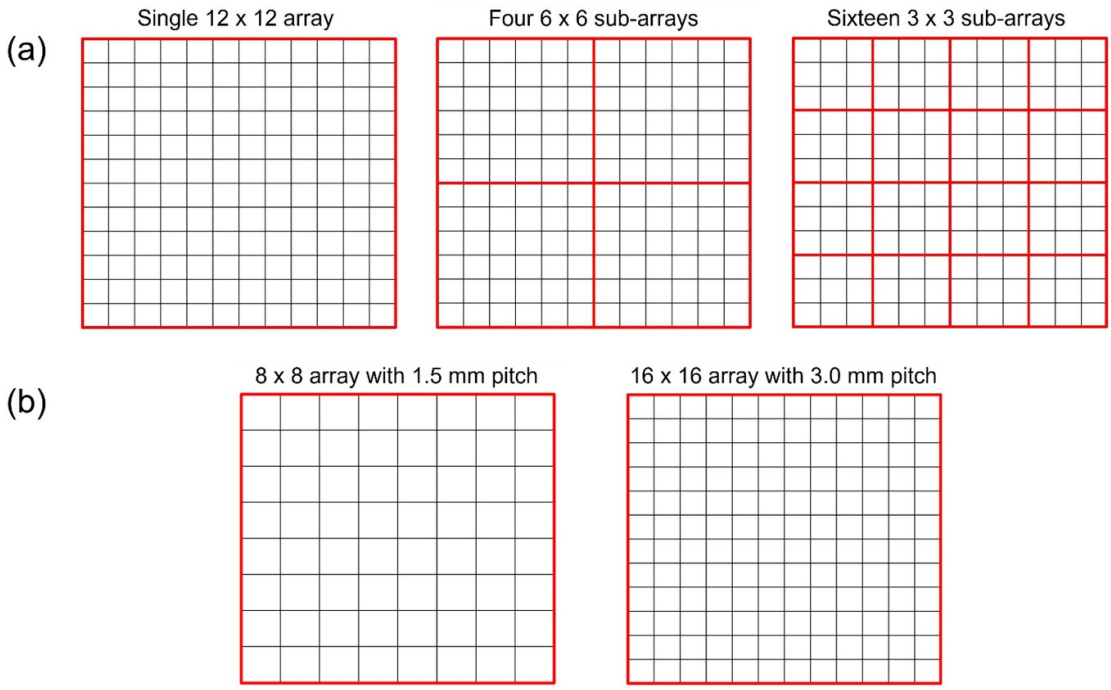

Figure 2. LYSO scintillation crystal blocks used for the experiments: (a) scenario 1, (b) scenario 2.

Table 1. Setup for scenario 1 and 2.

		Scenario 1		Scenario 2	
Crystal pitch		2 mm		1.5 mm	3 mm
# of compartment	Single	2 × 2	4 × 4	single	

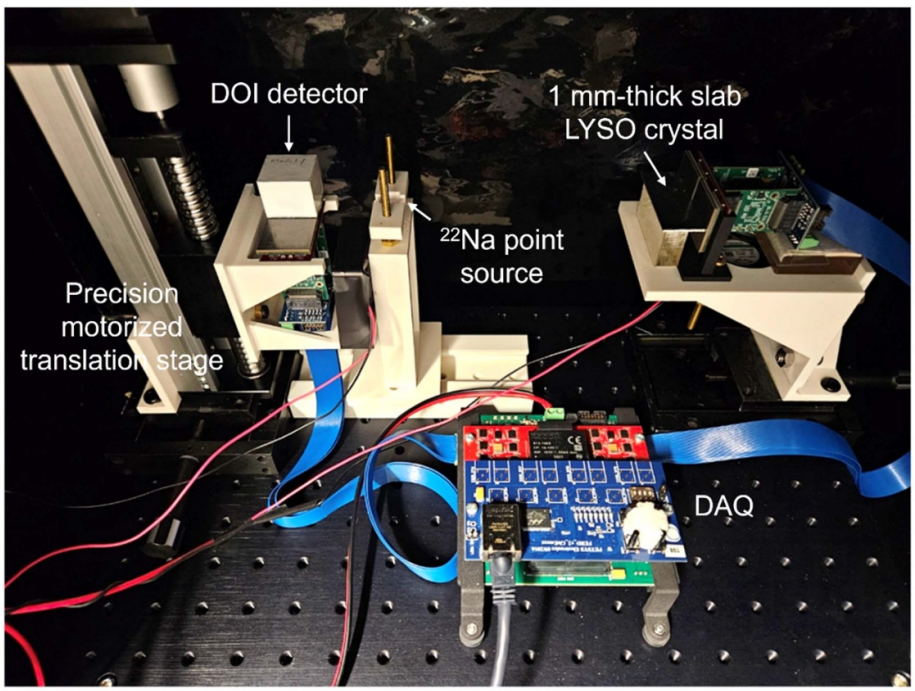

Figure 3. Experimental setup.

Signals from the SiPM array were processed through a PETsys FEB/D front-end board (PETsys Electronics, Portugal), which provides per-channel timestamping and charge integration (figure 3). For each configuration, approximately 1.5×10^6 valid coincidence events were collected to ensure sufficient statistical precision for depth classification. The resulting dataset for each geometry contained the 8×8 SiPM pixel responses for each event, along with the corresponding depth label defined by the mechanical position of the stage. To correct for small variations in optical coupling efficiency or photon yield, all events were normalized by their total signal intensity before further analysis.

2.3. DOI estimation algorithms

Five different algorithms were implemented to evaluate how the choice of decoding strategy influences DOI estimation across detector geometries. These included two conventional analytical metrics, a Euclidean-distance classifier, a Gaussian MLE and its modified variant, and a ANN. All algorithms used the same pre-processed dataset, in which each event was represented by the normalized 8×8 SiPM response matrix and its corresponding depth label.

The conventional analytical methods relied on simple statistical descriptors of the light distribution. Two scalar quantities were derived from the SiPM response: the variance and the max/sum ratio of the row- and column-projected signals. The DOI parameter D was defined as a linear combination of the two directional projections,

$$D = AX_i + Y_i \tag{1}$$

where A is a linear coefficient that balances the contributions of the horizontal and vertical components. Here, X_i and Y_i represent the DOI parameters obtained from the horizontal and vertical projections, respectively; when $i = 1$, the parameters correspond to the variance, and when $i = 2$, they correspond to the max/sum ratio. The coefficient A was swept from–3 to $+3$ to determine the optimal value. Two weighting strategies were considered: a crystal-specific coefficient optimized for each pixel and a single uniform coefficient applied to all crystals. These metrics served as a reference for evaluating more advanced decoding methods.

To simultaneously utilize both variance and max/sum as DOI metrics, a Euclidean-distance classification approach was employed. A scatter plot was generated in a two-dimensional feature space, where the variance was assigned to the x-axis (P) and the max/sum ratio to the y-axis (Q). The centroid positions corresponding to each known depth were determined from the training data, effectively forming five representative clusters. Each event was then assigned to the depth class whose centroid had the minimum Euclidean distance from the event position in the (P, Q) space (figure 4). This procedure provides a simple yet effective way to extend conventional DOI metrics into a multi-feature domain, allowing the variance and max/sum information to be jointly utilized for depth classification.

$$\widehat{\vec{z}} = \text{argmin} \left(\sqrt{B \times \left(\hat{P} - P(\vec{z})\right)^2 + \left(\hat{Q} - Q(\vec{z})\right)^2} \right). \tag{2}$$

The Gaussian MLE method treated the detector response at each pixel as a Gaussian distribution characterized by a mean value $\mu_i(z)$ and standard deviation $\sigma_i(z)$ at different depth z (i.e. 2, 6, 10, 14, and 18 mm). The most probable depth $\hat{z}$ was estimated by minimizing the negative log-likelihood of observing a given event s_i:

$$\widehat{\vec{z}} = \text{argmin} \sum_{i=1}^{16 \text{ or } 64} \left[\frac{(s_i - \mu_i(\vec{z}))^2}{2\sigma_i^2(\vec{z})} + \ln \sigma_i(\vec{z}) \right]. \tag{3}$$

The parameters $\mu_i(z)$ and $\sigma_i(z)$ were obtained from 70% of the dataset and later used to evaluate the remaining 30 %. Two input representations were tested: the full 8×8 SiPM response matrix and the 16×1 vector obtained from its row- and column-projected sums. To improve the robustness against non-Gaussian tails in the measured response, a modified MLE was also implemented by introducing a tunable hyper-parameter A that adjusts the weighting of the logarithmic term:

$$\widehat{\vec{z}} = \text{argmin} \sum_{i=1}^{16 \text{ or } 64} \left[\frac{(s_i - \mu_i(\vec{z}))^2}{2\sigma_i^2(\vec{z})} + C \ln \sigma_i(\vec{z}) \right]. \tag{4}$$

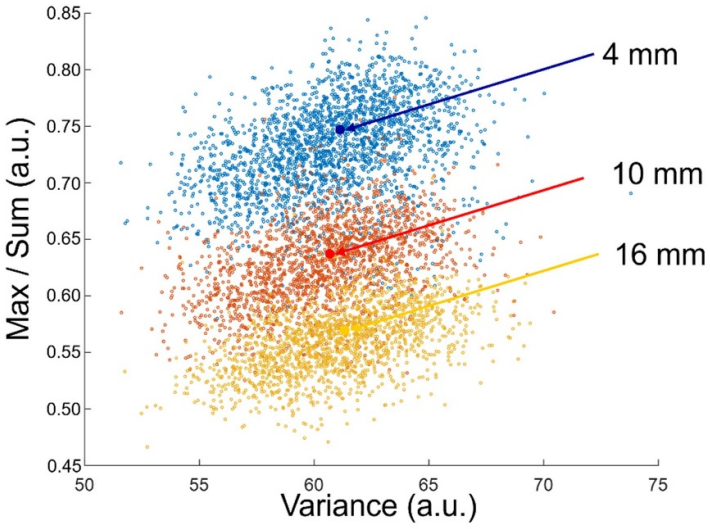

Figure 4. Euclidean distance from the event position in the (*P*, *Q*) space (*P*: variance, *Q*: max/sum).

Parameter C was optimized empirically to maximize DOI classification accuracy by sweeping from -10 to 10 with 0.1. This formulation provides additional flexibility when the light-distribution statistics deviate from an ideal Gaussian shape.

Finally, a fully connected ANN was constructed to explore data-driven DOI decoding. The model, which was designed in our previous study (Shim *et al* 2025), consisted of five hidden layers (2048-1024-512-256-256 nodes) with rectified linear unit activation functions and was implemented in PyTorch. The full 8×8 SiPM response matrix or the 16×1 row- and column-projected sums were used as input. The output layer produced class probabilities corresponding to discrete DOI depths—three for scenario 1 and five for scenario 2. Two training schemes were examined: (1) a *crystal-wise* model trained separately for each crystal position, allowing local adaptation to pixel-dependent light patterns, and (2) a *block-wise* model trained with events from all crystals to capture global features of the detector. All networks were trained with categorical cross-entropy loss and the Adam optimizer using 70% of the data, while the remaining 30% served as an independent test set.

2.4. Performance evaluation

The performance of each DOI decoding method was evaluated using two complementary metrics: (1) DOI resolution and (2) DOI classification accuracy. For conventional analytical metrics and Euclidean-distance classification, the DOI resolution, which has conventionally been used to quantify depth sensitivity in cDOI detectors, was defined as the FWHM of the reconstructed depth distribution at each known irradiation position. For each configuration, the reconstructed DOI parameter was histogrammed and fitted with a Gaussian function to extract the mean and FWHM values representing the DOI response and resolution, respectively. In contrast, methods based on probabilistic or data-driven classification—namely the MLE, modified MLE, and ANN—were evaluated in terms of DOI classification accuracy, defined as the percentage of correctly assigned depth classes relative to the total number of events. For the analytical and clustering-based approaches, continuous depth parameters were discretized into the same number of classes to enable comparison on an equal basis.

Because DOI resolution and classification accuracy represent different but related forms of depth-discrimination performance, the Euclidean-distance method was introduced as an intermediate approach to provide a quantitative bridge between the two evaluation domains. By mapping the variance and max/sum features into a two-dimensional space and classifying events based on their proximity to reference centroids, this method allowed indirect comparison between the conventional metric–based and classification-based estimators under a unified performance framework.

All analyses were carried out separately for each detector configuration and decoding algorithm to quantify the effects of light confinement. The resulting DOI resolution and accuracy values were then compared to identify the most effective combination of detector geometry and decoding strategy.

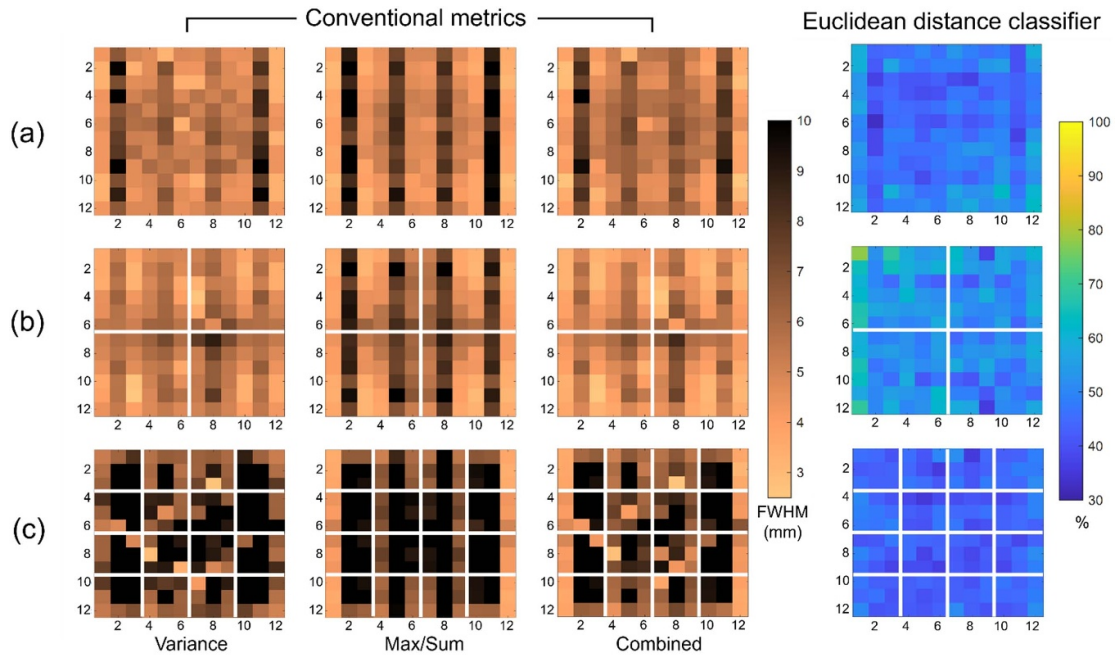

Figure 5. Performance (DOI resolution or accuracy) of conventional analytical metrics (variance, max/sum, combined, and Euclidean distance classifier) in scenario 1 to investigate the effect of array segmentation. (a) Single 12 × 12 array (b) Four 6 × 6 sub-arrays (c) Sixteen 3 × 3 sub-arrays.

3. Results

3.1. Scenario 1: effect of array segmentation

3.1.1. 1 × 1 segment configuration (unsegmented 12 × 12 array)

For the unsegmented detector block, the energy resolution was 13.5%. The DOI resolution obtained from the conventional analytical metrics was 5.5 ± 1.5 mm FWHM when calculated using the variance and 6.1 ± 2.0 mm FWHM when using the max/sum ratio (figure 5(a)). It was observed that both DOI parameters exhibited considerable variation in the linear coefficient for optimal DOI resolution among individual crystals, indicating a strong crystal-to-crystal dependency (figure 6(a), table 2). When using the max/sum ratio, the DOI resolution was notably degraded in columns 2, 5, 8, and 11. When, for each crystal, the better of the two parameters was selected (i.e. optimal per-crystal choice), the overall DOI resolution improved to 5.2 ± 1.7 mm FWHM. Using both parameters jointly in a two-dimensional (P, Q) space—where P denotes the variance and Q the max/sum—the Euclidean-distance classifier achieved 47.6 ± 5.7% accuracy. Likelihood-based decoding further enhanced depth discrimination (figure 7(a), table 2). The Gaussian MLE reached 59.9 ± 11.5% accuracy with the 8 × 8 pixel input and 65.1 ± 8.5% with the 8 rows + 8 columns projected input. The modified MLE increased these values to 73.7 ± 10.4% and 76.6 ± 7.1 %, respectively, indicating that re-weighting the logarithmic term better captures the non-Gaussian features of the measured light distributions.

The ANN provided the highest performance in this configuration (figure 8(a), table 2). With crystal-wise training, accuracies were 86.1 ± 5.6% (8 × 8 pixel input) and 85.2 ± 5.2% (8 rows + 8 columns projected input); with block-wise training, they were 87.6 ± 4.8% (8 × 8 pixel input) and 85.7 ± 4.3% (8 rows + 8 columns projected input).

3.1.2. 2 × 2 segment configuration (6 × 6 sub-arrays)

For 2 × 2 segment configuration, the energy resolution was 11.9%. The DOI resolutions obtained from the conventional analytical metrics were 4.8 ± 1.1 mm FWHM using the variance and 5.8 ± 1.9 mm FWHM using the max/sum ratio (figure 5(b)). The variation became less pronounced, but a similar tendency was observed, particularly with degraded DOI resolution at columns 2, 5, 8, and 11 for the max/sum ratio. When the optimal per-crystal choice strategy was applied, the overall DOI resolution improved to 4.7 ± 1.1 mm FWHM, representing the best performance among the three segmentation levels. The Euclidean-distance classifier achieved 53.2 ± 6.2% DOI classification accuracy.

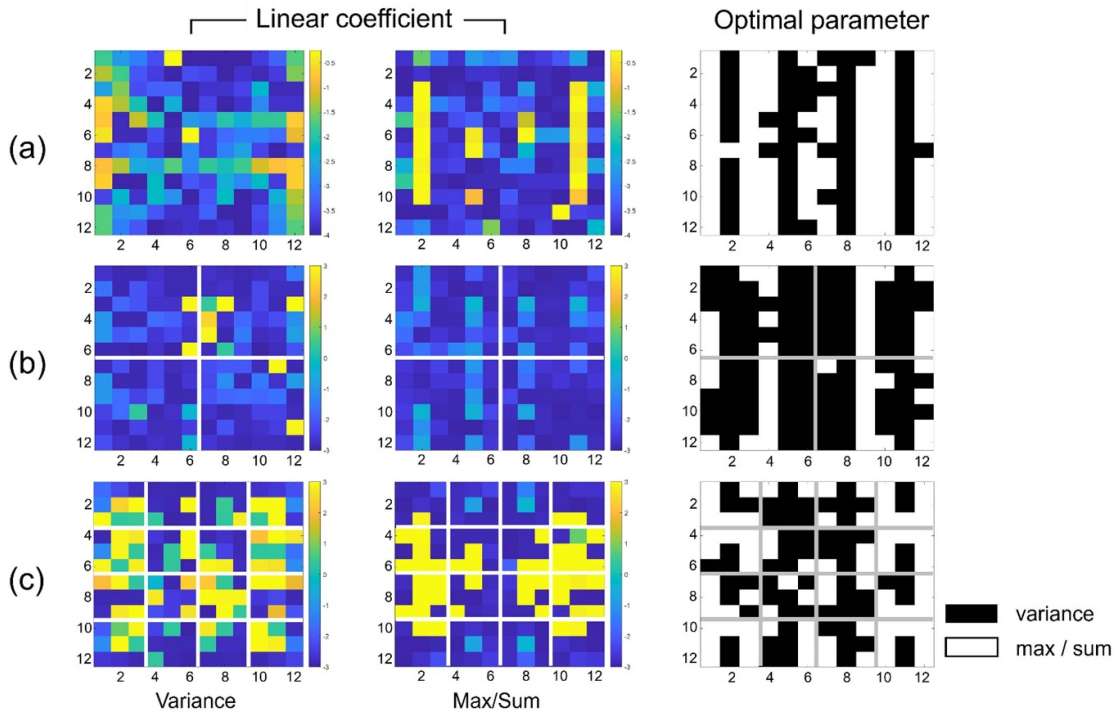

Figure 6. Optimal linear coefficients for variance and max/sum and optimal parameter maps in scenario 1. (a) Single 12 × 12 array (b) Four 6 × 6 sub-arrays (c) Sixteen 3 × 3 sub-arrays.

Table 2. DOI classification accuracy in scenario 1 to investigate the effect of array segmentation.

		Segment		
Methods	Input	1 × 1	2 × 2	4 × 4
Euclidean distance	Individual	47.6%	53.2%	43.5%
MLE	Individual	59.9%	58.2%	50.7%
	Row/column sum	65.1%	62.5%	52.0%
Modified MLE	Individual	73.7%	73.6%	64.3%
	Row/column sum	76.6%	77.0%	66.0%
ANN	Individual (crystal-wise)	86.1%	88.4%	82.1%
	Row/column sum (crystal-wise)	85.2%	86.9%	79.8%
	Individual (block-wise)	87.6%	89.0%	82.8%
	Row/column sum (block-wise)	85.7%	87.2%	80.5%

The Gaussian MLE achieved 58.2 ± 11.4% accuracy using the 8 × 8 pixel input and 62.5 ± 10.6% with the 8 rows + 8 columns projected input, while the modified MLE further increased these values to 73.6 ± 7.2% and 77.0 ± 6.7 %, respectively (figure 7(b), table 2).

The ANN achieved the highest performance across all decoding methods (figure 8(b), table 2). For crystal-wise training, accuracies were 88.4 ± 4.2% for the 8 × 8 pixel input and 86.9 ± 4.4% for the 8 rows + 8 columns projected input. When trained block-wise, the corresponding accuracies were 89.0 ± 4.0% and 87.3 ± 3.8 %, respectively. This configuration provided the best DOI decoding performance overall, achieving nearly 89% classification accuracy, which corresponds to an effective DOI resolution of 4.7 mm.

3.1.3. 4 × 4 segment configuration (3 × 3 sub-arrays)

For 4 × 4 segment configuration, the energy resolution was 10.2%. The DOI resolutions obtained from the conventional analytical metrics were 9.2 ± 2.0 mm FWHM using the variance and 10.0 ± 1.8 mm FWHM using the max/sum ratio (figure 5(c)). Both DOI parameters still exhibited considerable variation in the linear coefficient among individual crystals (figure 6(c), table 2). The optimal per-crystal resolution was 8.2 ± 1.9 mm FWHM, indicating a marked reduction in DOI discriminability compared

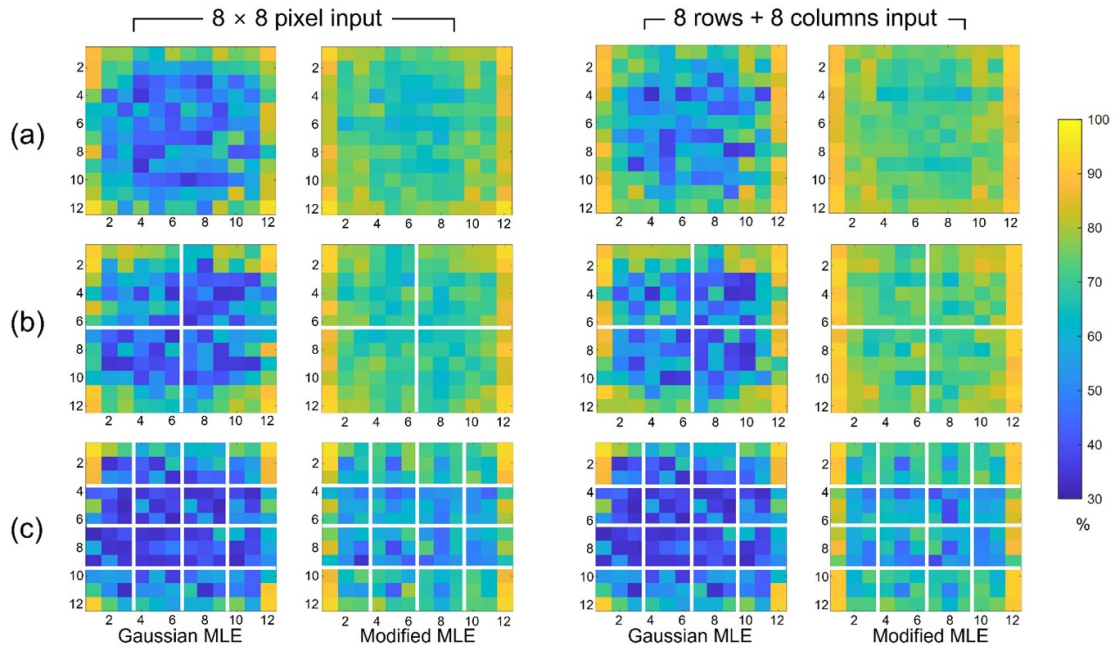

Figure 7. DOI accuracy of Gaussian and modified MLEs in scenario 1 (a) Single 12 × 12 array (b) Four 6 × 6 sub-arrays (c) Sixteen 3 × 3 sub-arrays.

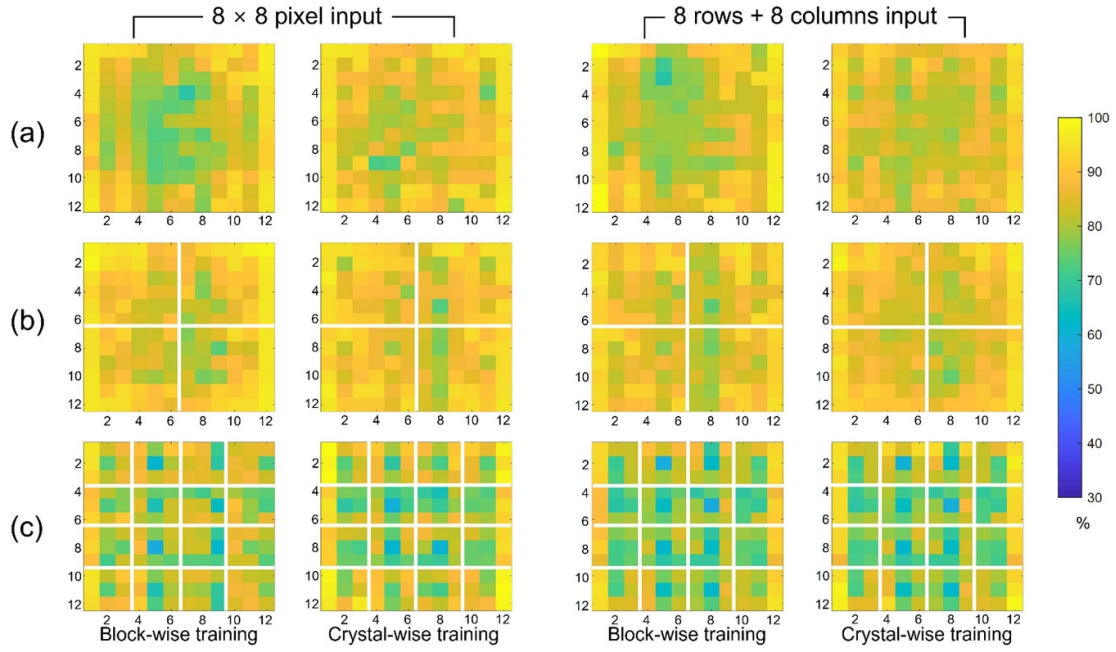

Figure 8. Performance (DOI accuracy) of ANNs in scenario 1 (a) Single 12 × 12 array (b) Four 6 × 6 sub-arrays (c) Sixteen 3 × 3 sub-arrays.

with the 2 × 2 segmented array. The Euclidean-distance classifier achieved the DOI classification accuracy of 43.5 ± 3.2 %.

The Gaussian MLE achieved 50.7 ± 10.2% accuracy with the 8 × 8 pixel input and 52.0 ± 9.8% with the 8 rows + 8 columns projected input, while the modified MLE improved these to 64.3 ± 8.1% and 65.7 ± 7.4 %, respectively (figure 7(c), table 2).

The ANN maintained the highest accuracy among all decoding methods, reaching 82.1 ± 6.3% and 79.8 ± 6.0% for crystal-wise training, and 82.8 ± 5.9% and 80.5 ± 5.7% for block-wise training, using the 8 × 8 pixel and 8 rows + 8 columns projected inputs, respectively (figure 8(c), table 2).

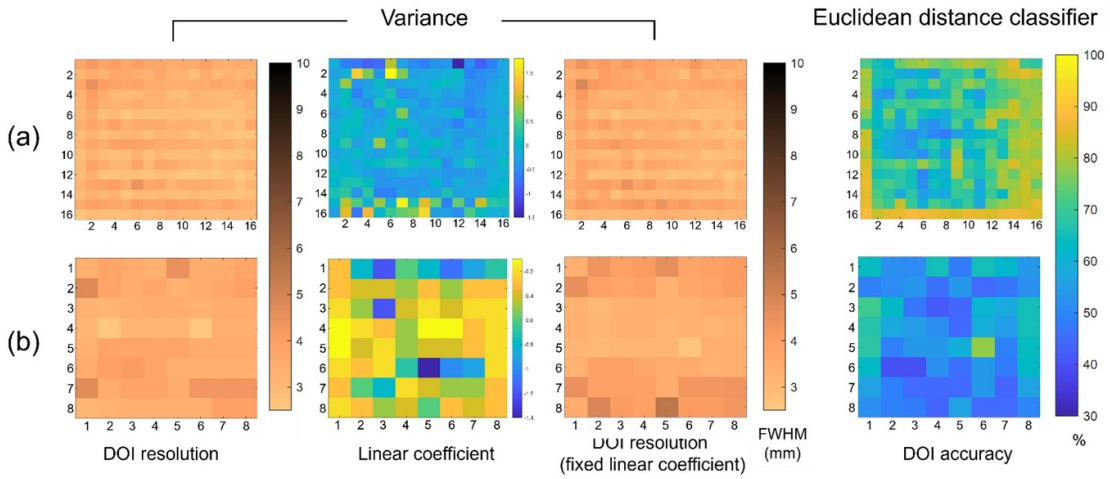

Figure 9. Performance of variance as DOI estimator and Euclidean distance classifier in scenario 2 to investigate the effect of increased optical interfaces. (a) 8 × 8 array with 1.5 mm pitch (b) 16 × 16 array with 3.0 mm pitch.

3.2. Scenario 2: effect of increased optical interfaces

3.2.1. 1.5 mm pitch array

For 1.5 mm pitch array, the energy resolution was 14.2%. When coefficient A was optimized separately for each crystal (crystal-wise optimal A), the DOI resolutions were 3.3 ± 0.4 mm FWHM for the variance-based parameter (figure 9(a)) and 4.5 ± 0.8 mm FWHM for the max/sum (figure 10(a), table 3). For all crystals, the variance parameter provided better DOI resolution than the max/sum ratio. When a single coefficient was uniformly applied across all crystals (global A), the best results were obtained at $A = -0.1$ for the variance parameter and $A = -0.2$ for the max/sum parameter, yielding DOI resolutions of 3.4 ± 0.4 mm and 4.7 ± 1.1 mm FWHM, respectively. The Euclidean-distance classifier achieved 69.8 ± 10.5% DOI classification accuracy.

The Gaussian MLE achieved accuracies of 55.3 ± 11.2% (8 × 8 input) and 64.0 ± 8.9% (8 rows + 8 columns projected input), while the modified MLE improved these to 61.7 ± 8.6% and 68.7 ± 7.4 %, respectively (figure 11(a), table 3).

The ANN decoder achieved the highest performance, with accuracies of 82.9 ± 5.0% and 82.0 ± 4.8% for crystal-wise training, and 82.3 ± 5.4% and 81.4 ± 5.6% for block-wise training, using the 8 × 8 pixel and 8 rows + 8 columns inputs, respectively (figure 12(a), table 3).

3.2.2. 3 mm pitch array

For 3 mm pitch array, the energy resolution was 11.1%. With the crystal-wise optimal A, the DOI resolutions were 3.6 ± 0.5 mm FWHM for the variance parameter (figure 9(b)) and 4.4 ± 0.8 mm FWHM for the max/sum parameter (figure 10(b), table 3). Across all crystals, the variance parameter consistently yielded better DOI resolution compared with the max/sum ratio. With global A, the best performance was obtained at $A = -0.3$ for the variance parameter and $A = -0.9$ for the max/sum parameter, resulting in DOI resolutions of 3.7 ± 0.6 mm and 4.4 ± 0.7 mm FWHM, respectively. The Euclidean-distance classifier achieved 56.4 ± 8.2% DOI classification accuracy.

The Gaussian MLE achieved accuracies of 49.8 ± 7.8% (8 × 8 input) and 58.6 ± 10.2% (8 rows + 8 columns projected input), while the modified MLE improved these to 58.0 ± 7.1% and 66.2 ± 7.4 %, respectively (figure 11(b), table 3).

The ANN again produced the highest performance, with accuracies of 82.0 ± 5.3% and 81.2 ± 5.4% for crystal-wise training, and 81.8 ± 5.8% and 81.3 ± 5.0% for block-wise training, using the 8 × 8 pixel and 8 rows + 8 columns inputs, respectively (figure 12(b), table 3).

4. Discussions

4.1. Summary of DOI performance

4.1.1. Scenario 1 (effect of array segmentation)

The 2 × 2 segmented detector exhibited the best overall performance, achieving an optimal DOI resolution of 4.7 mm FWHM (figure 5(b)) and an ANN classification accuracy of approximately 89%

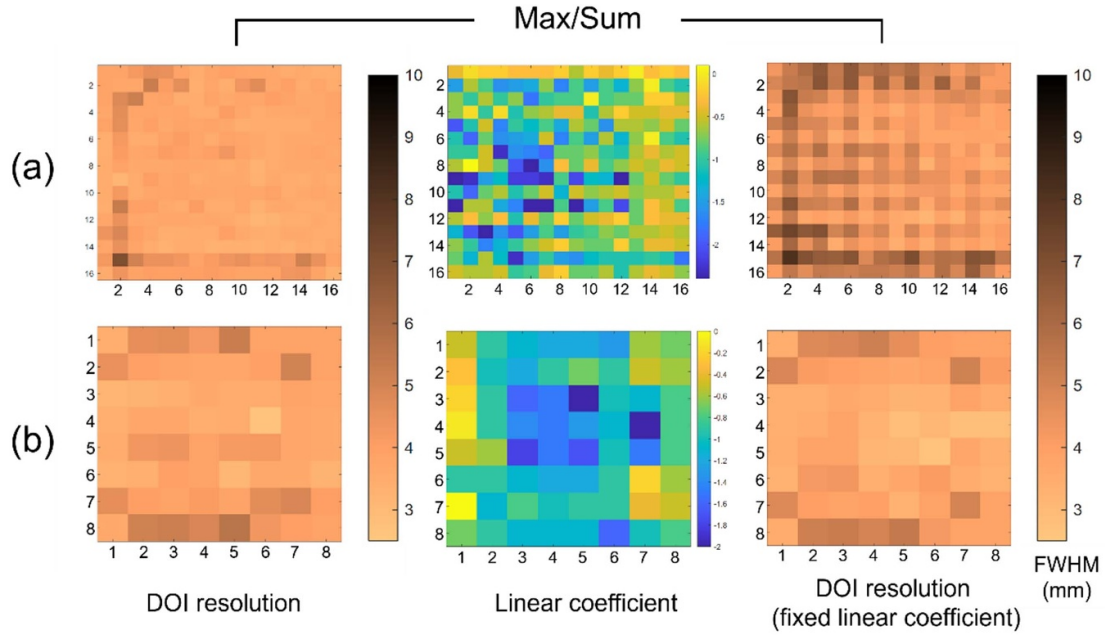

Figure 10. Performance of max/sum as DOI estimator in scenario 2. (a) 8 × 8 array with 1.5 mm pitch (b) 16 × 16 array with 3.0 mm pitch.

Table 3. DOI classification accuracy in scenario 2 to investigate the effect of increased optical interfaces.

		Pitch	
Methods	Input	1.5 mm	3 mm
Euclidean distance	Individual	69.8%	56.4%
MLE	Individual	55.3%	49.8%
	Row/column sum	64.0%	58.6%
Modified MLE	Individual	61.7%	58.0%
	Row/column sum	68.8%	66.2%
ANN	Individual (crystal-wise)	82.9%	82.0%
	Row/column sum (crystal-wise)	82.0%	81.3%
	Individual (block-wise)	82.3%	81.8%
	Row/column sum (block-wise)	81.4%	81.4%

(figure 7(b), table 2). The unsegmented configuration produced slightly lower yet stable performance (≈5.2 mm (figure 5(a)), 87% (figure 7(a), table 2)), whereas excessive segmentation (4 × 4) caused clear degradation (≈8.2 mm (figure 5(c)), 82% (figure 7(c), table 2)). This trend indicates that moderate segmentation enhances DOI encoding by improving the edge signal-to-noise ratio of the light-distribution gradient while maintaining spatial continuity of photon propagation.

4.1.2. SCENARIO 2 (effect of increased optical interfaces)

Both configurations (1.5 mm and 3.0 mm) achieved comparable DOI resolutions of ≈3.3–3.7 mm (figure 9) and accuracies of ≈82%–83% (figure 12). Between them, the 1.5 mm-pitch detector achieved the better performance, indicating that increased optical interfaces allows more accurate encoding of the depth-dependent light distribution within the SiPM array.

4.1.3. Comparison with other PET detector systems

In a previous study using a reflector configuration similar to that of the present work (Lee *et al* 2017), DOI resolutions of 4.28 ± 0.32 mm and 4.24 ± 0.28 mm FWHM were reported for 1.47 mm-pitch crystals. Another study using triangular reflectors (Nadig *et al* 2023) reported 2.0 mm RMSE (not FWHM). Even under the ideal assumption of zero bias, this corresponds to 4.71 mm FWHM, and the equivalent FWHM would be even larger if bias were present. In another study that measured DOI using non-triangular gap structures (Yu *et al* 2024), a DOI resolution of 3.0 mm FWHM was achieved

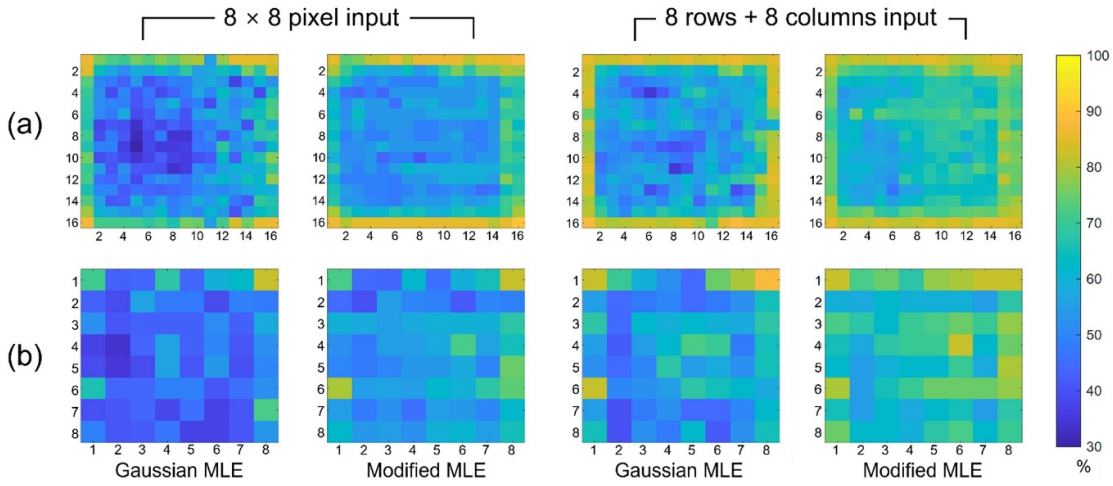

Figure 11. Performance of Gaussian and modified MLEs in scenario 2. (a) 8 × 8 array with 1.5 mm pitch (b) 16 × 16 array with 3.0 mm pitch.

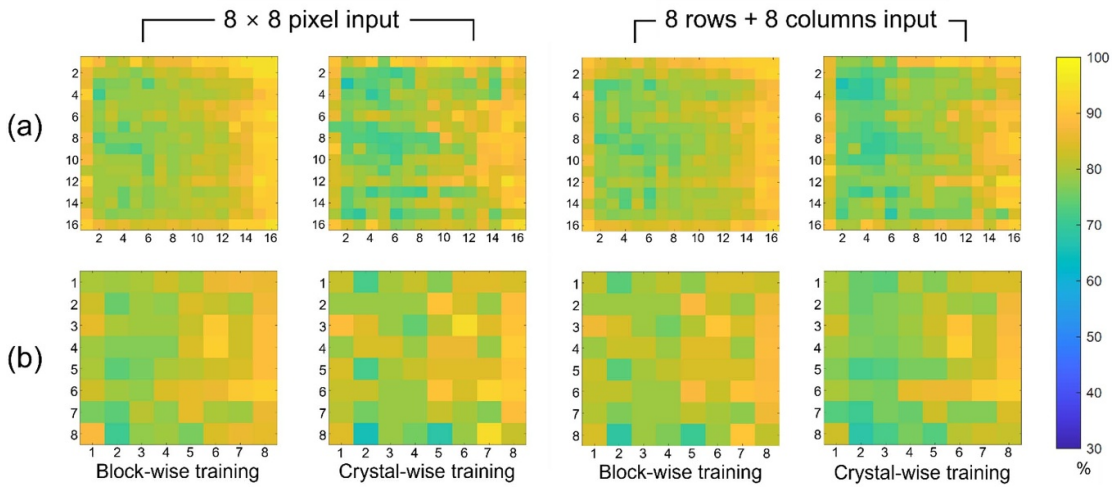

Figure 12. Performance of ANNs in scenario 2. (a) 8 × 8 array with 1.5 mm pitch (b) 16 × 16 array with 3.0 mm pitch.

for 2 mm-pitch crystals. Although this represents strong performance, the method had the limitation that DOI could not be estimated for the four corner crystals. The apparent state-of-the-art result was reported by LaBella *et al* (2020a), which achieved 2.5 mm FWHM for 1.4 mm-pitch crystals; however, this approach required an additional prism-shaped light guide.

4.2. Interpretation of optical and algorithmic mechanisms

4.2.1. Optical light-distribution behavior

From an optical standpoint, as light confinement increased, DOI performance peaked under moderate confinement but deteriorated at stronger confinement, whereas energy resolution improved continuously due to enhanced light-collection efficiency. In the unsegmented configuration, photons spread laterally across a wide area, generating a continuous but shallow light-distribution gradient that enables stable DOI decoding but results in relatively lower energy resolution due to a lower SNR in the regions with fewer detected photons. Introducing moderate segmentation (2 × 2) confined the photon paths within each sub-array, enhancing both the gradient contrast for DOI and SNR, which improved energy resolution from 13.46% to 11.94 %. When the segmentation became stronger to 4 × 4, photon confinement increased further, resulting in the best energy resolution, 10.22 %, owing to efficient light collection, but DOI sensitivity deteriorated because the lateral light-sharing continuity was lost. This opposite trend between DOI and energy resolution highlights the fundamental trade-off between optical confinement and depth encoding capability.

A similar tendency was observed in the second scenario. When the crystal and SiPM pitches were closely matched, the number of optical interfaces decreased, reducing photon losses caused by interfacial crosstalk and thereby improving energy resolution from 14.23% to 11.14% as the pitch increased from 1.5 mm to 3.0 mm. However, the finer 1.5 mm pitch provided slightly superior DOI resolution because the denser optical sampling allowed more detailed encoding of the depth-dependent light-distribution gradient, even with lower photon-collection efficiency. Overall, these findings suggest that light-confinement geometry primarily influences energy resolution, whereas the smoothness of the light-distribution gradient plays a key role in DOI sensitivity.

Overall, the 2 mm-pitch configurations in scenario 1 exhibited lower DOI resolution and accuracy than those in scenario 2. This trend is likely due to the mis-alignment between the SiPMs and the crystal array. The DOI degradation observed in specific columns (2, 5, 8, and 11) can be explained by the fact that the crystals in these columns are positioned at the boundary between two SiPMs. As a result, the scintillation light from the crystal producing the largest number of photons is divided between adjacent SiPMs, thereby degrading DOI performance.

4.2.2. Response of DOI decoding algorithms

The decoding algorithms responded differently to these optical characteristics. The analytical metrics (variance and max/sum) directly depend on the monotonicity and smoothness of the light-distribution gradient, making them sensitive to distortions introduced by segmentation or photosensor gaps.

The Gaussian MLE models the detector response statistically but assumes a symmetric unimodal distribution, limiting its adaptability when the light pattern becomes asymmetric or discontinuous. The modified MLE improves robustness by introducing a flexible weighting factor that compensates for local deviations from the Gaussian model, yielding moderate enhancement in classification accuracy.

Recently, artificial intelligence technologies have become the mainstream in medical image processing and analysis (Lee 2021, Bousse *et al* 2024, Kim *et al* 2024a, 2024b). Moreover, their application for improving the performance and reducing the readout complexity of PET detectors are increasing (Berg and Cherry 2018, Gong *et al* 2020, Decuyper *et al* 2021, Lee and Lee 2021, Onishi *et al* 2022, Ullah and Levin 2022, Shim *et al* 2023). The ANN decoder does not rely on explicit functional assumptions in contrast to the other methods used in this study. By learning nonlinear spatial correlations among SiPM pixels, the ANN effectively interprets complex and irregular light-distribution patterns, reconstructing depth information even when optical confinement is nonideal. This capability explains the ANN's consistent superiority across all geometries—it can extract depth-encoding features that are inaccessible by analytical or parametric statistical methods, maintaining high DOI accuracy under a wide range of optical conditions.

4.3. Experimental uncertainties and limitations

Several experimental factors may have affected the measured DOI performance. First, subtle differences in optical coupling and reflector alignment among detector configurations could have modified the effective light-distribution profile. Although optical grease was applied consistently, small local variations in contact pressure or microscopic air gaps between the crystal and the SiPM array may have influenced photon transmission efficiency.

Second, the depth-dependent measurements were performed using electrical collimation, in which a slab-type reference detector defined the coincidence acceptance window along the depth direction. Because the reference crystal had a finite thickness and nonuniform lateral sensitivity, the effective beam width differed slightly between the left and right sides of the detector. This asymmetry in the coincidence geometry could lead to small differences in the reconstructed DOI resolution across lateral positions. To mitigate the influence of scattered events, energy histograms were generated for each crystal pixel, and DOI was estimated using only events within a predefined energy window; the energy resolution reported for each configuration represents the average across individual crystal pixels, such that scattered events were considered to be effectively excluded. It should be noted, however, that once scattering occurs, the true irradiation point cannot be accurately identified, and estimating DOI using an oblique beam under face-on irradiation inherently involves inferring depth indirectly from the lateral position, introducing an additional source of uncertainty in the reference DOI. For detector-level studies where side-on irradiation is feasible, it represents a more direct approach for assessing DOI performance, and we plan to establish a mechanically collimated experimental setup to address this limitation in future work.

Third, minor fluctuations in SiPM gain or bias voltage during acquisition may have slightly affected the SiPM output signal amplitude (Lee and Hong 2010) and, consequently, the DOI metrics derived

from variance and max/sum. Although the acquisition electronics were stabilized and regularly calibrated, small variations in operating bias could still contribute to sub-millimeter differences in reconstructed DOI resolution.

Finally, this study focused exclusively on DOI characterization under controlled optical and electronic conditions. Other detector performance aspects, such as timing or gain variation per pixel, were not explicitly optimized.

5. Conclusions

This study comprehensively analyzed how optical geometry and decoding algorithms jointly determine DOI performance in single-ended cDOI detectors. By systematically varying the degree of optical confinement, we demonstrated that appropriate optical confinement has yielded better DOI precision. The algorithmic evaluation showed that neural decoders effectively have recovered depth information. These results establish practical design principles for cDOI detectors: properly controlling light confinement is important for maximizing DOI resolution, and data-driven decoding provides a robust framework for exploiting these optimized optical features in future PET detector designs.

Data availability statement

The data cannot be made publicly available upon publication because the cost of preparing, depositing and hosting the data would be prohibitive within the terms of this research project. The data that support the findings of this study are available upon reasonable request from the authors.

Author contributions

Hyeong Seok Shim
Conceptualization (lead), Formal analysis (lead), Investigation (lead), Methodology (lead), Resources (equal), Software (lead), Writing – original draft (lead), Writing – review & editing (lead)

Min Jeong Cho
Software (equal)

Wen He
Resources (supporting)

Min Sun Lee 0000-0002-1442-2285
Supervision (supporting)

Craig S Levin
Supervision (equal)

Jae Sung Lee 0000-0001-7623-053X
Funding acquisition (lead), Supervision (equal)

References

Berg E and Cherry S R 2018 Using convolutional neural networks to estimate time-of-flight from PET detector waveforms *Phys. Med. Biol.* **63** 02LT01

Bousse A, Kandarpa V S S, Shi K, Gong K, Lee J S, Liu C and Visvikis D 2024 A review on low-dose emission tomography post-reconstruction denoising with neural network approaches *IEEE Trans. Radiat. Plasma Med. Sci.* **8** 333–47

Decuyper M, Stockhoff M, Vandenberghe S and Van Holen R 2021 Artificial neural networks for positioning of gamma interactions in monolithic PET detectors *Phys. Med. Biol.* **66** 075001

Du H, Yang Y, Glodo J, Wu Y, Shah K and Cherry S R 2009 Continuous depth-of-interaction encoding using phosphor-coated scintillators *Phys. Med. Biol.* **54** 1757

Du J, Bai X and Cherry S R 2019 Performance comparison of depth-encoding detectors based on dual-ended readout and different SiPMs for high-resolution PET applications *Phys. Med. Biol.* **64** 15nt03

Gong K, Berg E, Cherry S R and Qi J 2020 Machine learning in PET: from photon detection to quantitative image reconstruction *Proc. IEEE.* **108** 51–68

Hong S J, Kwon S I, Ito M, Lee G S, Sim K-S, Park K S, Rhee J T and Lee J S 2008 Concept verification of three-layer DOI detectors for small animal PET *IEEE Trans. Nucl. Sci.* **55** 912–7

Ito M, Hong S J and Lee J S 2011 Positron emission tomography (PET) detectors with depth-of-interaction (DOI) capability *Biomed. Eng. Lett.* **1** 70–81
Ito M, Lee J S, Kwon S I, Lee G S, Hong B, Lee K S, Sim K S, Lee S J, Rhee J T and Hong S J 2010a A four-layer DOI detector with a relative offset for use in an animal PET system *IEEE Trans. Nucl. Sci.* **57** 976–81
Ito M, Lee J S, Park M-J, Sim K-S and Hong S J 2010b Design and simulation of a novel method for determining depth-of-interaction in a PET scintillation crystal array using a single-ended readout by a multi-anode PMT *Phys. Med. Biol.* **55** 3827
Ito M, Lee M S and Lee J S 2013 Continuous depth-of-interaction measurement in a single-layer pixelated crystal array using a single-ended readout *Phys. Med. Biol.* **58** 1269–82
Kim S, Park H and Park S-H 2024a A review of deep learning-based reconstruction methods for accelerated MRI using spatiotemporal and multi-contrast redundancies *Biomed. Eng. Lett.* **14** 1221–42
Kim W, Jeon S-Y, Byun G, Yoo H and Choi J-H 2024b A systematic review of deep learning-based denoising for low-dose computed tomography from a perceptual quality perspective *Biomed. Eng. Lett.* **14** 1153–73
LaBella A, Cao X, Petersen E, Lubinsky R, Biegon A, Zhao W and Goldan A H 2020a High-resolution depth-encoding PET detector module with prismatoid light-guide array *J. Nucl. Med.* **61** 1528–33
LaBella A, Zhao W, Lubinsky R and Goldan A H 2020b Prismatoid light guide array for enhanced gamma ray localization in PET: a Monte Carlo simulation study of scintillation photon transport *Phys. Med. Biol.* **65** 18lt01
Lee J S 2021 A review of deep-learning-based approaches for attenuation correction in positron emission tomography *IEEE Trans. Radiat. Plasma Med. Sci.* **5** 160–84
Lee J S and Hong S J 2010 *Geiger-mode Avalanche Photodiodes for PET/MRI. Electronics for Radiation Detection* (K. Iniewski, CRC Press) pp 179–99
Lee M S, Kim K Y, Ko G B and Lee J S 2017 Prototype pre-clinical PET scanner with depth-of-interaction measurements using single-layer crystal array and single-ended readout *Phys. Med. Biol.* **62** 3983–96
Lee M S and Lee J S 2015 Depth-of-interaction measurement in a single-layer crystal array with a single-ended readout using digital silicon photomultiplier *Phys. Med. Biol.* **60** 6495–514
Lee S and Lee J S 2021 Inter-crystal scattering recovery of light-sharing PET detectors using convolutional neural networks *Phys. Med. Biol.* **66** 185004
Lewellen T K, Janes M and Miyaoka R S 2004 DMice-a depth-of-interaction detector design for PET scanners *IEEE Nucl. Sci. Symp. Med. Imaging Conf. Rec.* **1** 2388–92
Moses W W and Derenzo S E 1994 Design studies for a PET detector module using a PIN photodiode to measure depth of interaction *IEEE Trans. Nucl. Sci.* **41** 1441–5
Nadig V, Gundacker S, Schug D, Herweg K, Weindel K, Radermacher H, Mueller F, Weissler B and Schulz V 2023 Scalable, time-of-flight and depth-of-interaction detector units for high-resolution PET systems *IEEE Trans. Radiat. Plasma Med. Sci.* **8** 1–14
Onishi Y, Hashimoto F, Ote K and Ota R 2022 Unbiased TOF estimation using leading-edge discriminator and convolutional neural network trained by single-source-position waveforms *Phys. Med. Biol.* **67** 04NT01
Seo M, Park H, Lee S, Ko G B and Lee J S 2023 Depth-of-interaction positron emission tomography detector with 45° tilted silicon photomultipliers using dual-ended signal readout *Med. Phys.* **50** 4112–21
Shim H S, Cho M J, Lee M S and Lee J S 2025 Continuous single-ended depth-of-interaction measurement using highly multiplexed signals and artificial neural networks *Phys. Med. Biol.* **70** 035004
Shim H, Bae S, Lee S and Lee J 2023 Inter-crystal scattering event identification using a novel silicon photomultiplier signal multiplexing method *Phys. Med. Biol.* **68** 115008
Son J W, Lee M S and Lee J S 2017 A depth-of-interaction PET detector using a stair-shaped reflector arrangement and a single-ended scintillation light readout *Phys. Med. Biol.* **62** 465–83
Tsuda T, Murayama H, Kitamura K, Yamaya T, Yoshida E, Omura T, Kawai H, Inadama N and Orita N 2004 A four-layer depth of interaction detector block for small animal PET *IEEE Trans. Nucl. Sci.* **51** 2537–42
Ullah M N and Levin C S 2022 Application of artificial intelligence in PET instrumentation *PET Clin.* **17** 175–82
Yi M, Ko G B and Lee J S 2024 Pushing the limit of BGO-based dual-ended Cherenkov PET detectors through photon transit time correction *Phys. Med. Biol.* **69** 025005
Yoshida E, Obata F, Kamada K, Yoshikawa A and Yamaya T 2021 Development of crosshair light sharing PET detector with TOF and DOI capabilities using fast LGSO scintillator *Phys. Med. Biol.* **66** 225003
Yu X, Zhang X, Zeng J, Zhang Y, Zhao H, Tao J, Zhu Z, Xu J, Xie S and Peng Q 2024 Depth of interaction in PET detector design: performance optimization with light-sharing window *IEEE Trans Instrum Meas.*